HHS Public Access

Author manuscript

Biomaterials. Author manuscript; available in PMC 2018 January 01.

Published in final edited form as:

Biomaterials. 2017 January ; 115: 155–166. doi:10.1016/j.biomaterials.2016.11.019.

YAP-dependent Mechanotransduction is Required for Proliferation and Migration on Native-like Substrate Topography

Shamik Mascharak,
Department of Bioengineering, Stanford University, Stanford, CA 94305

Patrick L. Benitez,
Department of Bioengineering, Stanford University, Stanford, CA 94305

Amy C. Proctor,
Department of Chemical Engineering, Stanford University, Stanford, CA 94305

Christopher M. Madl,
Department of Bioengineering, Stanford University, Stanford, CA 94305

Kenneth H. Hu,
Department of Biophysics, Stanford University, Stanford, CA 94305

Ruby E. Dewi,
Department of Materials Science and Engineering, Stanford University, Stanford, CA 94305

Manish J. Butte [Prof.], and
Department of Pediatrics, Stanford University, Stanford, CA 94305

Sarah C. Heilshorn* **[Prof.]**
Department of Materials Science and Engineering, Stanford University, Stanford, CA 94305

Abstract

Native vascular extracellular matrices (vECM) consist of elastic fibers that impart varied topographical properties, yet most *in vitro* models designed to study the effects of topography on cell behavior are not representative of native architecture. Here, we engineer an electrospun elastin-like protein (ELP) system with independently tunable, vECM-mimetic topography and demonstrate that increasing topographical variation causes loss of endothelial cell-cell junction organization. This loss of VE-cadherin signaling and increased cytoskeletal contractility on more topographically varied ELP substrates in turn promote YAP activation and nuclear translocation, resulting in significantly increased endothelial cell migration and proliferation. Our findings identify YAP as a required signaling factor through which fibrous substrate topography influences cell behavior and highlights topography as a key design parameter for engineered biomaterials.

heilshorn@stanford.edu, Postal address: 476 Lomita Mall, Stanford, CA 94305.

Keywords

cell matrix interactions; substrate topography; mechanotransduction signaling; electrospinning

1. Introduction

The native vascular extracellular matrix (vECM) is a complex network of fibrous biopolymers and interstitial space that varies widely in local mechanical, biochemical, and topographical properties. [1] This variation is thought to mediate local endothelial cell (EC) signaling to promote vascular tissue homeostasis and regeneration. [2] While the signaling pathways that mediate endothelial cell responses to mechanical and biochemical matrix cues have been deeply studied using both native and engineered biomaterials,[3–6] the mechanisms by which cells respond to topographical matrix cues are less well known. *In vivo*, elastin assembles into nanoscale fibrils that further assemble into micron-scale fibers with widths ranging from 500 nm to 4 μm. [7–10] As shown by scanning electron microscopy and histological study of rat aortas (Figure S1), these micron-scale fibers form the undulating internal elastic lamina upon which the basolateral surface of the endothelium sits. [9, 10] The quiescent, stable vascular endothelium sits on this planar mesh of micron-scale fibrous bundles[9], while angiogenic sprouts traverse a mesh of wider fibers surrounding the blood vessels. [10]

These anatomical features support the development of materials with micron-scale fibers to probe cellular interactions with the resulting topographical features.[3] Given the *in vivo* association between wider fibers and less quiescent behavior from ECs, it is reasonable to hypothesize that topographical variation may drive a functional cell transition towards migration and proliferation. While several studies have confirmed that ECs are responsive to engineered topographical signals,[11–13] the model surfaces employed have not been representative of native, fibrous vECM geometries. Furthermore, the underlying mechanism for EC topographical signal transduction remains largely unknown.[14] Previous work has not addressed whether topographical features actively induce phenotypic transition via biochemical signaling or play an exclusively passive role, e.g. by physically obstructing monolayer formation.[15] Importantly, many model topographical substrates hinder mechanistic insight by simultaneously altering multiple material parameters, confounding causal relationships. Carefully engineered and biologically relevant models are essential for investigating the role of matrix topography while controlling for the mechanical and biochemical cues that also affect endothelial phenotype.

2. Results and Discussion

2.1. Protein engineered fabrics enable orthogonal control over substrate topography

We investigated the effect of fibrous, vECM-mimetic topography on EC migration and proliferation using electrospun recombinant elastin-like protein (ELP) matrices. The electrospun material is reminiscent of vascular microarchitecture, with constituent fibers of similar shape and length scale as native vECM fibers (Figure 1 and Figure S2).[3, 8, 16] The ELP polymer contains multiple repeats of an elastin-derived structural sequence, imparting

elasticity, native-like mechanics, and facile crosslinking via glutaraldehyde linkage of lysine residues.[16, 17] A cell-adhesive RGD ligand was interspersed with the elastin-like amino acid sequence to enable integrin-mediated cell-fiber interactions (Figure S2a).[6] Specifically, we utilize a 17-amino acid peptide sequence derived from fibronectin that was previously demonstrated to engage the $\alpha_v\beta_3$ integrin on ECs when presented in ELP matrices.[6, 16, 18, 19] Importantly, full-length fibronectin and splice-variant CS fibronectin, which can engage multiple integrins including $\alpha_5\beta_1$ and $\alpha_4\beta_1$, are implicated in endothelial inflammation. In contrast, the RGD minimal cell-adhesive peptide ligand has been broadly investigated in a multitude of engineered biomaterial systems *in vitro* and *in vivo* to promote formation of a quiescent endothelial cell monolayer. [20–24] To tune fiber width, we varied the ELP mass fraction in the electrospinning solution. More concentrated ELP solutions resist jet elongation and thinning during electrospinning, leading to wider fiber matrices with greater topographical relief.

Consistent with previous work, electrospun ELP fibers were ribbon-like in cross-section and closely resembled native vECM (Figure S2b).[6, 16] Spinning solutions with 27%, 34%, and 40% w/w aqueous ELP yielded fibers with average widths of ~0.8, 1.2, and 2.0 μm, respectively (Figure 1a and 1b). Multiple layers of fibers were spun to form a cohesive fabric and to minimize the possibility of EC contact with the underlying glass coverslip. Quantitative evaluation of the fiber width distribution for each matrix confirmed minimal overlap between the distributions of the narrowest and widest fibers for each condition (Figure S3a), and the mean fiber widths were significantly different. In contrast, the distribution of fiber heights did not significantly vary with ELP mass fraction (Figure S3b). Two parameters were used to quantify the extent of topographical variation on the micron scale: arc-chord ratio and average z-plane deviation from the mean (Figure S4). This topographical variation occurs at a length scale similar to that of individual cells, permitting optical characterization by confocal microscopy. As can be visually appreciated from x-z/y-z orthogonal projections (Figure 1a), ELP fabrics composed of larger fibers had more topographical variation and hence a statistically significant increase in both arc-chord ratio and average z-plane deviation (Figure 1c and 1d). This range of electrospun fiber widths (0.8–2.0 μm) and resulting topographical variation (arc-chord ratios of 1.2–1.8) are similar to those observed in histological sections of rat aortas (fiber width ~1.5 μ and arc-chord ratio of 1.6, Figure S1). This affirmed ELP fiber width as an ideal parameter to tune surface topography.

Density of accessible RGD ligands[25, 26] and matrix mechanical properties[3, 4, 27, 28] are both correlated with cell proliferation, spreading, and motility. We therefore confirmed that these parameters were comparable for each fiber width. We estimated that increasing fiber width from 0.8 to 2.0 μm resulted in a small decrease in ligand density from 19,200 RGD μm^{-2} to 17,600 RGD μm^{-2} (Figure S5b and Experimental Section). This small change in accessible ligand density is not expected to be biologically relevant, given our previous work demonstrating that at least a doubling of RGD ligand density is required for significant changes in EC phenotype on ELP fabrics. [6] To experimentally verify that this small decrease was not biologically meaningful, human umbilical vein endothelial cells (HUVEC) were cultured on each topographical condition for two days and immunostained for vinculin, an adaptor protein associated with focal adhesion formation in response to RGD ligand

binding. The number of focal adhesions per cell (see Experimental Section) did not significantly vary amongst fiber width conditions (Figure S6), suggesting no significant change in the number of accessible RGD ligands. The fabric swelling ratio, void fraction, and bulk tensile mechanics were also not significantly different between the fabrics (Figure S7). The elastic modulus was approximately 150 kPa for all materials (Figure S7c), which is within the empirical range of moduli for whole vascular tissue at rest. [29] We also employed atomic force microscopy microindentation to characterize the elastic modulus on an individual fiber basis. Here too, no significant difference was noted between fiber width conditions (Figure S7d), confirming that topography could be tuned independently of intrinsic mechanics in the ELP matrices.

2.2. Topographical variation influences actin organization in a VE-cadherin dependent manner

To investigate whether variation in substrate topography affects the basolateral membrane, HUVEC were seeded onto varied fiber width ELP matrices and labeled for cytoplasm, nuclei, and VE-cadherin to assess individual cell and junction morphology. ELP-adsorbed PDMS substrates with stiffness values matched to electrospun fabrics were used as flat control substrates (see Experimental Section). For all fibrous substrates tested, the ECs remained on the top surface of the fabrics, and they were never observed to infiltrate into the fabric interior. Orthogonal projections of confocal micrographs showed that ECs on flat control and narrow fiber substrates spread laterally and in a planar manner, whereas their counterparts on larger fibers spread less in plane but adopted a more uneven basolateral membrane (Figure 1e). To quantify this observation, we calculated arc-chord ratio and average z-plane deviation of the basolateral membrane and found that they closely matched values of fibers alone (Figure 1c and 1d), indicating a close association between cells and fibers.

As expected, VE-cadherin morphology was similar on small-diameter, fibrous ELP matrices (*i.e.* with low topographical variation) and flat control ELP matrices (Figure 2C) and was consistent with confluent, quiescent EC monolayers on other flat engineered substrates.[30–32] However, on closer inspection of confocal micrographs and orthogonal projections, we noted a striking loss of VE-cadherin on more topographically varied substrates (white arrow, Figure 1e and Figure 2a top panels) that closely resembled the morphological effects of a VE-cadherin blocking antibody (Figure 2a bottom panels). Quantification (see Experimental Section) revealed a dramatic 4-fold increase in junction disruption between the smallest and largest fiber widths (Figure 2c). Thus, a modest increase in size scale of the underlying fibrous topography was sufficient to block VE-cadherin organization into adherens junctions, despite otherwise identical culture conditions. In the vascular endothelium, junction proteins such as VE-cadherin are critical regulators of the actin cytoskeleton (Figure S8).[27, 33, 34] To investigate actin organization, HUVEC seeded onto varied topographies were labeled for F-actin filaments. While ECs on ELP substrates with low topographical variation showed actin filaments organized into strong cortical arcs (indicative of mature cell-cell contacts; white arrow, Figure 2b top panels), ECs on matrices with high topographical variation displayed large, spanning stress fibers. This same cytoskeletal rearrangement occurred on all substrates after treatment with a VE-cadherin blocking

antibody (Figure 2b bottom panels). Supporting this result, we found that projected cell spread area and nuclear area both decreased roughly 2-fold with increasing fiber width (Figure 2d and 2e). This decrease in projected cell spread area on fabrics with greater topographical variation was accompanied by a modest increase in basolateral contact surface area between the cells and the substrate (Supporting Information). Contractile stresses drive shape changes at both the organelle and cellular length scales.[35, 36] A similar trend in whole-cell and nuclear area was noted across all substrates after treatment with a VE-cadherin blocking antibody. Collectively, these data indicated that loss of VE-cadherin-mediated cell-cell junctions on ELP matrices with high topographical variation led to reorganization of the actin cytoskeleton to a more contractile configuration.

2.3 Loss of VE-cadherin organization on topographically varied substrates promotes endothelial migration and proliferation

In addition to influencing morphology, VE-cadherin is a master regulator of cell behavior and signaling during contact inhibition, which is characterized by a phenotypic shift towards quiescence (i.e., slow motility, cell cycle arrest) when individual ECs contact each other.[37] To assess collective cellular motility, we tracked cellular movement over 16 hours by time-lapse microscopy. ECs moved at significantly higher speeds on 2.0 μm matrices relative to flat control, 0.8, and 1.2 μm-wide fibrous substrates. In addition, ECs moved at significantly higher speeds on all substrates after VE-cadherin antibody blocking, as expected for cells relieved of contact inhibition (Figure 3a and 3b). Using tracked centroid positions, we calculated mean correlation distance as a global parameter of cell-cell coordination. This value reports the average radial distance at which individual cell movements ceased to influence neighboring cell movements (Figure S9). Correlation distance decreased sharply with increasing topographical variation and across all substrates after VE-cadherin antibody blocking, from roughly 30 nm to 8 nm (Figure 3c), confirming that loss of cell-cell junctions promoted more individualistic, random motility. We measured EC proliferation by immunostaining for cell cycle entry-associated protein Ki67 and quantifying the fraction of Ki67-positive cells (i.e., growth fraction). Similar to motility speed, the EC growth fraction rose sharply with increasing fiber width and after addition of a VE-cadherin blocking antibody (Figure 3d and 3e), suggesting that loss of VE-cadherin signaling can lead to increased proliferation on more topographically varied substrates. Overall, these significant changes in motility and proliferation implied that greater topographical variation induced a monolayer-wide increase in individualistic motility and proliferation through a loss of adherens junctions. In the native vasculature, weakening of cell-cell junctions is a key step in sprouting angiogenesis, as it enables cells to divide, dissociate from the monolayer, and explore surrounding tissues.[18, 38]

2.4 Topography-mediated disruption of VE-cadherin organization is dependent on Rho, ROCK, and Rac signaling

We next looked to establish a causative mechanism linking substrate topography and loss of endothelial quiescence. Given the observed relationship between junction integrity and cytoskeletal contractility, we hypothesized that inhibition of Rho, ROCK, and Rac signaling would reinstate the non-contractile, quiescent phenotype noted on flat ELP and smaller width ELP fibers. Small GTPases Rho, Rac and downstream effector ROCK regulate actin

rearrangement during stress fiber formation, contraction, and lamellipodial protrusion. [39] We employed a family of three different cytoskeletal inhibitors, Rhosin; Y-27632; and IPA-3, with functionally distinct points of action to inhibit Rho, Rac, and Racl/PAKl, respectively (Figure S8). A qualitative and quantitative regain of VE-cadherin junction integrity was noted on 2.0 μ matrices upon cytoskeletal inhibition (Figure 4a left panels and 4b). Correspondingly, Rho, ROCK, and Rac-inhibited ECs on larger width fibers showed strong cortical actin arcs reminiscent of untreated ECs on smaller fibers (white arrow, Figure 4a right panels). For ECs on matrices with greater topographical variation (i.e. larger fiber widths), cytoskeletal inhibition resulted in greater cell spreading (Figure 4c) and larger nuclear cross-sectional areas (Figure 4d). This increase in cell spreading upon cytoskeletal inhibition corresponded with a change in EC morphology, with the cells spreading over the fabric surface in a 2D planar manner rather than following the 3D topographical contours of the fabric (Figure S10). Interestingly, for ECs on flat ELP control substrates an opposite response was observed; EC spread area decreased after cytoskeletal inhibition, consistent with previously reported results.[40, 41] This observation suggests that conventional relationships between cell spread area and contractility may not readily translate from planar 2D substrates to substrates with 3D topographical contours. Collectively, these findings suggested that topographical variation stimulates the endothelium, causing Rho/ROCK/Rac-dependent cytoskeletal reorganization and loss of VE-cadherin junction integrity. Together with the observed increase in contractility after VE-cadherin antibody blocking (Figure 2b), these data also suggested that the reorganization of actin and loss of VE-cadherin during the transition away from quiescence are self-reinforcing. Topographical variation-induced cytoskeletal contractility drives loss of VE-cadherin, which in turn stimulates further cytoskeletal contractility (indicated by a double-headed arrow in Figure S8). To demonstrate that the morphological shift towards quiescence described above was functionally relevant, we quantified the Ki67 growth fraction for ECs seeded onto varied topographies and treated with Rho, ROCK, and PAK-1 inhibitors. Across all conditions, cytoskeleton inhibition resulted in significantly lower growth fraction (Figure 4e and 4f). In contrast, no decrease in growth fraction was observed on flat control surfaces, suggesting that cytoskeletal inhibition did not introduce a nonspecific bias towards quiescence by blocking the cell cycle. Thus, regulators of cytoskeletal organization are required for topography-mediated transition away from the quiescent EC phenotype.

2.5 Disruption of VE-cadherin organization by fibrous topography supports mechanotransduction signaling by YAP

Given the array of signaling roles that VE-cadherin plays,[38, 42–44] we sought to identify a specific cell-cell junction-dependent effector explaining the observed shift away from quiescence on larger width fibers. Recently, the Hippo transcriptional co-activator Yes-associated protein (YAP) was shown to mediate endothelial quiescence in concert with VE-cadherin through two separate pathways (Figure S11).[31, 44] In both pathways, phosphorylation results in inactivation of cytoplasmic YAP. In contrast, activated YAP translocates to the nucleus, where it induces expression of genes involved in angiogenic sprouting and vascular remodeling. [44] To assess YAP activation in response to topographical cues, we immunostained ECs cultured on flat control and varied fiber width ELP matrices for YAP and quantified the fraction localized to the nucleus (see Experimental

Section). A fiber width increase from 0.8 to 2.0 μ was associated with a roughly 20% enrichment of YAP to the nucleus (Figure 5a and 5b). When ECs were seeded at a lower density (thereby increasing junction disruption across all substrates, Figure S12), nuclear enrichment of YAP rose across all substrates (Figure 5b). In contrast, when ECs were seeded at higher density, nuclear enrichment of YAP decreased. Treatment of ECs with ROCK inhibitor Y-27632 decreased nuclear YAP roughly 50% across all substrates (Figure 5b and 5c), as expected given that F-actin filaments prevent LATS1/2-mediated inactivation of YAP (Figure S11). Finally, disruption of VE-cadherin junctions with VE-cadherin blocking antibody increased nuclear YAP localization across all substrates to levels near that of 2.0 μm matrices (Figure 5b and 5c left panels). These findings suggested that activation of YAP on more topographically varied ELP substrates was specifically caused by the decrease in cell-cell junction integrity.

Next, we assessed whether YAP activation on larger width fibers was associated with the observed increase in cellular proliferation. ECs on varied diameter matrices were co-immunostained for YAP and Ki67. Across all topographical conditions, Ki67+ cells showed roughly 20% higher localization of YAP to the nucleus than Ki67- cells (70% vs. 50%, respectively, Figure 5d left panel). Activated YAP binds enhancer regions across the genome via TEAD factors.[45] To confirm that cell cycle entry was specifically promoted by YAP-TEAD interactions, we treated ECs with the chemical inhibitor Verteporfin, previously shown to inhibit YAP signaling by disrupting the YAP-TEAD complex.[46] Interestingly, a rise in nuclear YAP was observed across all topographical conditions after treatment with Verteporfin, possibly as a feedback response to signaling-incompetent YAP. However, nuclear translocation of YAP did not correlate with an increase in cellular proliferation in Verteporfin-treated ECs. Both ECs that stained positively and negatively for nuclear Ki67 showed the same degree of nuclear YAP localization (Figure 5d right panel), suggesting that cell cycle entry in Verteporfin-treated ECs was likely promoted by other factors.

Finally, to investigate this change in intracellular YAP localization on a biosignaling level, we measured total expression and phosphorylation of FAK (focal adhesion kinase) and the MAPK (mitogen-activated protein kinase) family member ERK1/2 by Western blotting. We found no significant changes in total expression of FAK, ERK1/2 or phosphorylation of FAK (Figure 5e). The lack of changes in FAK expression and phosphorylation supported our vinculin morphology data showing that changing fibrous topography in this model did not alter focal adhesion formation. In contrast, phosphorylation of the MAPK family protein ERK1/2 showed a 5-fold increase from the smallest to largest fiber width (Figure 5e). ERK is a well-known phosphorylation target of several pro-angiogenic factors regulated by YAP-TEAD, including angiopoetin-2, and is associated with increased motility and proliferation in response to mitogenic and migratory ECM signaling. [44, 47, 48]

2.6 Topography-induced endothelial migration and proliferation requires YAP

Our findings identified YAP as a topography-sensitive effector associated with endothelial migration and proliferation. However, they did not explicitly suggest whether YAP was *necessary* for these responses. To probe YAP's specific contribution towards topography-induced EC migration, we tracked ECs seeded onto varied topographies after 24 hours of

treatment with YAP-TEAD inhibitor Verteporfin. Surprisingly, ECs on all substrates showed significantly slower motility after YAP-TEAD inhibition with no apparent cell death (Figure 6a and 6b). This result demonstrates that YAP was necessary for EC motility in our system. To probe YAP's specific contribution to EC proliferation, we measured the growth fractions of both untreated ECs and VE-cadherin blocked ECs after either siRNA-mediated YAP knockdown (Figure S13) or Verteporfin-mediated inhibition of YAP-TEAD interaction. Consistent with previous results, ECs transfected with control siRNA and treated with VE-cadherin blocking antibody proliferated at a high rate on all topographies due to a lack of contact inhibition (Figure 6c upper left panel and 6d). In contrast, ECs transfected with YAP siRNA proliferated at a very low level, even after antibody-mediated disruption of VE-cadherin (Figure 6c right panels and 6d). A similar result was found for ECs treated with Verteporfin (Figure 6c bottom left panel and 6e).

Collectively, these data indicated that YAP activation is necessary for topography-mediated transition of the model endothelium towards a more highly proliferative and migratory phenotype. To our knowledge, this is the first example demonstrating the central role of YAP in transduction of native-like topographical cues. Given that cadherins and YAP are present in a variety of tissue types and appear to be significantly affected by substrate topography, we expect this finding to have broad implications for monolayer physiology. These data suggest that biomaterial topography could be used to promote the development of *in vitro*, tissue-engineered vascular networks, which are being explored for a variety of applications ranging from toxicological screening to clinical ischemia therapy.[49–51] As endothelial cell-cell junctions and basolateral interactions with the substrate can be altered under flow conditions, such as those experienced *in vivo* due to blood flow, future studies should evaluate the combinatorial effects of substrate topography and fluid shear stress on endothelial physiology. In future studies, it will be important to elucidate the biophysical mechanisms linking fibrous substrate topography to cytoskeletal contractility. Marked deformation of the basolateral cell membrane and the close association between fibers and ECs seemed to indicate that larger fibers induced more bending and focal curvature of the cell membrane.[52] It is possible that curved EC membranes bear greater in-plane tensile forces, linking positive membrane curvature to increased cytoskeletal contractility.

3. Conclusion

Here, we orthogonally tuned the biochemical, mechanical, and topographical properties of a vascular-ECM mimetic, electrospun ELP substrate. This engineered material enabled the discovery that substrate topography disrupts endothelial quiescence and promotes migration and proliferation. These cell responses to substrate topography were determined to be a result of enhanced cytoskeletal contractility, loss of VE-cadherin organization, YAP activation, and subsequent interactions between YAP and TEAD (Figure S11). Consistent with this novel mechanistic hypothesis, chemical disruption of Rho, ROCK, Rac, and YAP signaling blocked endothelial migration and proliferation on topographically varied ELP substrates. Significantly, these findings demonstrate that the range of fiber widths found in the vECM may be sufficient to trigger phenotypic changes in endothelial monolayers without any exogenous biochemical factors typically associated with the transition away from quiescence, and highlight native-like substrate topography as a critically important

matrix signal regulating cell morphology, signaling, and behavior. Our results also support the use of topography as a design parameter for implantable biomaterials to regulate cellular migration and proliferation.

4. Experimental Section

Elastin-like protein (ELP) expression and purification

As previously reported, ELP was expressed and purified using standard recombinant technology.[17] Two ELP variants were synthesized, a cell-adhesive protein termed RGD-ELP, which includes a fibronectin-derived RGD ligand within the sequence, and a non-cell-adhesive protein termed RDG-ELP, which includes a scrambled version of the ligand that is not bioactive.[6, 17] Genes encoding the desired protein sequences were assembled within pJ401 plasmids using gene assembly (DNA 2.0) and traditional recombinant techniques. *Escherichia coli* strain BL21 Star (DE3) pLysS was transformed with the ELP plasmid for expression. Bacteria were cultured to OD600 of 0.6 (37 °C, LB medium, 1.5 L) in baffled flasks on a shaker (300 rpm). The culture was used to inoculate a fed-batch fermenter (Bioengineering, Inc.), grown to OD600 of 3 on batch medium (37 °C, pH 6.8, Terrific Broth plus 20 g L^{-1} glucose, 30 L), then grown to OD600 of 20 on feed (500 g L^{-1} glucose, 13 g L^{-1} ammonium chloride, 5.5 g L^{-1} magnesium sulfate, 9 mL/min) before inducing expression with 1 mM P-isopropyl thiogalactoside. Expression (34 °C) was allowed to continue for 2 days. The wet cell pellet obtained after ELP expression was resuspended in TEN Buffer (1 g/mL, 1 mM PMSF), subjected to three freeze-thaw cycles, and digested with DNAse I. The suspension was adjusted to pH 3 with 5 N HC1, incubated at 4 °C for 1 h, and centrifuged at 4 °C (1 h, 22,000 g). The supernatant was harvested and NaCl was added to a final concentration of 0.2 M. This solution was agitated at 40 °C, shaken for 3 h, and centrifuged at 40 °C (1 h, 22,000 g). After decanting, the pellet was resuspended in water (0.2 g/mL), agitated overnight at 4 °C, and centrifuged at 4 °C (1 h, 8,000 g). Warm (40 °C, 0.2 M NaCl, 8,000 g) and cold (4 °C, 8,000 g) purification cycles were each repeated five times. The final supernatant was desalted by dialyzing into water (4 °C, 3,000 MWCO) and lyophilized for a minimum of 4 days. Protein yield was approximately 200 mg L^{-1}.

Electrospinning ELP matrices

Recombinant ELP proteins were dissolved overnight in deionized water (4 °C) at specified fractions of ELP mass to total mass (ELP and water). RGD ligand density was specified at a constant value of 18,000 μm^{-2} (see example calculation in Electrospun ELP Characterization section) within electrospun ELP fabrics by blending bioactive RGD-ELP with non-bioactive RDG-ELP in a 13:87 percent mass ratio for all fiber size conditions (Figure 1). To produce fabric matrices, solutions were electrospun (200 μL h^{-1} flow rate, room temperature) onto aminated glass coverslips (12-mm diameter). Aminated glass was prepared by reacting glass coverslips (28 g) in aqueous silination solution (10 μM 3-aminopropyltrimethoxysilane and 5% v/v acetic acid in 50 mL) for 30 min, sequentially rinsing with pure ethanol and water, and drying. Electrospinning conditions were as follows: 27% ELP (3 h, 14 kV, 16 cm, hydrated by placing a solution of saturated potassium chloride in the chamber overnight), 34% ELP (70 min, 15 kV, 15 cm, ambient humidity), and 40% ELP (35 min, 16 kV, 14 cm, unit desiccated overnight). To reduce pre-steady state artifacts,

solutions were allowed to run for 2 min before exposure to the electric field. All electrospun coatings were fabricated to be at least 10 μm in depth, and fiber density was evaluated by quantitatively assessing the fabric void fraction (see details in *Electrospun ELP Characterization* section). After electrospinning, matrices on coverslips were cut from the rest of the deposited material in 12-mm diameter circles and crosslinked. To crosslink, matrices were placed in a vacuum chamber along with two room-temperature solutions (20 mL each) in separate 10-cm petri dishes. One, a solution of water saturated with potassium chloride, was used to control chamber humidity. Two, a 50% v/v solution of glutaraldehyde in water, provided the crosslinking reagent. After placing matrices and solutions in the chamber, the chamber was sealed by vacuum. Vapor-phase glutaraldehyde reacted with primary amines on ELP lysine residues (4 h).[16] Chemical crosslinking of the bottom-most fibers to the aminated glass surface prevented delamination of electrospun fabrics from their respective coverslips. Crosslinking was completed by sequentially hydrating fabrics with aqueous 5 M and 1 M sodium chloride, each for 10 min at 37 °C, as previously reported. [16] Unreacted glutaraldehyde was quenched by treating fabrics with 0.3 M glycine (aqueous, 37 °C, 2 h). Crosslinking of ELP matrices imparts long-term aqueous stability with minimal loss of protein over the course of days. [16] Flat control substrates were prepared by hole-punching 12-mm, 1:28 Sylgard 184 PDMS disks (125 kPa elastic modulus matches the stiffness of crosslinked ELP fabrics), which were then plasma-treated for 30 sec and incubated in 1 mM RGD-ELP solution overnight. Substrates were sterilized overnight by incubating in 70% ethanol and irradiating with ultraviolet light. As reported previously, this sterilization procedure does not impact biofunctionality of the RGD tripeptide within ELP fabrics. [6] Before culture, exposed glass and PDMS was blocked (4% w/v bovine serum albumin (BSA), 37° C, 2 h).

Electrospun ELP characterization

For measurements of fiber width, fabric void fraction, and topographical variation, phosphate-buffered saline (PBS) hydrated matrices were imaged with a Leica SPE confocal microscope using autofluorescence of crosslinked ELP fibers with a 1-μm step size in the z-axis to a total depth of at least 10 μm. ImageJ was used for quantification of all images. For fiber width analysis, 200 individual fibers were measured for each substrate. Void fraction was defined as the three-dimensional open volume within the fabric relative to the total fabric volume. Void fraction was quantified over 3 different z-stacks for each substrate by measuring the open volume (*i.e.*, sum of open areas between fibers for each z-stack slice multiplied by slice height) and dividing by the total fabric volume (*i.e.*, total image area multiplied by total z-stack height). Topographical variation was calculated as both the average arc-chord ratio and average z-plane deviation using orthogonal x-z/y-z cross-sections of the materials (Figure S4). Differences between fiber width distributions were statistically significant by ANOVA with Tukey-Kramer *post-hoc* test. Differences for all other data, unless specified otherwise, were evaluated by Student's t-test.

Ligand presentation properties—Using the measured aspect ratios (Figure S3), we modeled fibers as 500 nm thick ribbons with a uniform distribution of ligands. Ligands were considered accessible if they were within 23 nm of the fiber surface, corresponding to the length of the heterodimeric, extracellular portion of the $\alpha_v\beta_3$ integrin.[53] For each fiber

width, the material swell ratio was approximately 12 (wet mass by dry mass, Figure S7a), so the average density of total protein matrix was nearly constant. The void fraction of each matrix was approximately 0.33 (Figure S7b); together with the unchanging swell ratio, this indicated that the relative amounts of aqueous buffer inside and outside of the fibers were similar for each fiber condition. An example calculation for 1.2 μm wide fibers is included below.

Convert bulk mass swell ratio $(12\frac{\mathrm{g\ \ wet}}{\mathrm{g\ \ dry}})$ to bulk elastin volume fraction:

$$(1\mathrm{g}*\frac{1\mathrm{mL\ \ elastin}}{1.35\mathrm{g\ \ elastin}})/(11\mathrm{g\ \ water}*\frac{1\mathrm{mL\ \ water}}{1\mathrm{g\ \ water}}+1\mathrm{g\ \ elastin}*\frac{1\mathrm{mL\ \ elastin}}{1.35\mathrm{g\ \ elastin}}=6.3\%\frac{\mathrm{mL\ \ elastin}}{\mathrm{mL\ \ bulk}}$$

Using fiber volume fraction $(58\%\frac{\mathrm{mL\ \ fibers}}{\mathrm{mL\ \ bulk}})$ and bulk elastin volume fraction, calculate fiber volume swell ratio:

$$\frac{6.3\%\frac{\mathrm{mL\ \ elastin}}{\mathrm{mL\ \ bulk}}}{58\%\frac{\mathrm{mL\ \ fibers}}{\mathrm{mL\ \ bulk}}}=0.11\frac{\mathrm{mL\ \ elastin}}{\mathrm{mL\ \ fiber}}$$

Convert fiber volume swell ratio to elastin density in fibers:

$$0.11\frac{\mathrm{mL\ \ elastin}}{\mathrm{mL\ \ fiber}}*1.35\frac{\mathrm{g\ \ elastin}}{\mathrm{mL\ \ elastin}}=0.15\frac{\mathrm{g\ \ elastin}}{\mathrm{mL\ \ fiber}}*10^{12}\frac{\mathrm{pg}}{\mathrm{g}}*10^{-12}\frac{\mathrm{mL}}{\mu\mathrm{m}^3}=0.15\frac{\mathrm{pg\ \ elastin}}{\mu\mathrm{m}^3\mathrm{fiber}}$$

Convert to [RGD], assuming fiber is 13% RGD-containing elastin (0.52 fmol RGD/fmol elastin):

$$0.15\frac{\mathrm{pg\ \ elastin}}{\mu\mathrm{m}^3\mathrm{fiber}}*\frac{\mathrm{fmol\ \ elastin}}{33.3\mathrm{pg\ \ elastin}}*\frac{0.52\mathrm{fmol\ \ RGD}}{\mathrm{fmol\ \ elastin}}*\frac{\mathrm{mol}}{10^{15}\mathrm{fmol}}*\frac{6.02*10^{26}}{\mathrm{mol}}=\frac{2.9*10^6}{\mu\mathrm{m}^3\mathrm{fiber}}$$

Calculate accessible [RGD] (surface concentration):

$$\frac{2.9*10^6}{\mu\mathrm{m}^3\mathrm{fiber}}*0.023\mu\mathrm{m}=\frac{65*10^3}{\mu\mathrm{m}^2\mathrm{fiber}}$$

Calculate effective, accessible [RGD] for cells sitting on a fabric:

$$\frac{65*10^3}{\mu\mathrm{m}^2\mathrm{fiber}}*58\%\frac{\mu\mathrm{m}^2\mathrm{fiber}}{\mu\mathrm{m}^2\mathrm{matrix}}*50\%(\mathrm{undersides\ \ of\ \ fibers\ \ are\ \ in\ \ accessible})=\frac{18*10^3}{\mu\mathrm{m}^2\mathrm{matrix}}$$

FAs from different cells were distinguished using actin and VE-cadherin co-stains to delineate whole cell and cell-cell boundaries (Figure S6a). The number of focal adhesions per EC was then calculated using an automated MATLAB script, as previously reported. [6]

Focal adhesions in Figure S6a and S6b that appear to be uncorrected with fibers were located at the bottom of the z-stack, so the associated fibers beneath them were not included in the z-stack used to generate the max projection. This was necessary since inclusion of all autofluorescent fibers would obscure the FA staining, making image analysis and visual inspection impossible.

Mechanical properties—For bulk tensile testing, freestanding matrices (2 mm × 15 mm) of varied fiber diameter were cut from the electrospinning deposition plate, crosslinked, and hydrated as described above. Matrices were then mounted with a gap of 4 mm and stretched at room temperature while hydrated in PBS until rupture using an Instron 5848 (2 mm/min). Tensile modulus was calculated from stress-strain curves as the slope of the best-fit line. For microscale tensile testing, crosslinked ELP matrices of varied diameter on glass coverslips were mounted to Fluorodish petri dishes, immersed in PBS and probed by Atomic Force Microscopy (AFM). To avoid piercing the soft fibers, SHOCON colloidal AFM probes (5–9 nm colloid diameter) were used in contact mode indentation to generate 20 × 20 matrices (2.5 μm × 2.5 μm) of force curves on each fiber size condition in triplicate (1 μm/s indentation speed, 150 pN force trigger). Force curves were fitted to the Hertzian indentation model to extract individual fiber elastic moduli.

Endothelial cell culture

Before seeding discrete monolayers, matrices on coverslips were dried under laminar airflow for 4 hours after blocking glass with BSA. Human umbilical vein endothelial cells (HUVEC, between passages 5 and 7) were grown to confluence, trypsinized, and then placed on dried matrices in three discrete 4-uL drops of 3,000 HUVEC μL^{-1} cell suspensions, as previously described. [54] The monolayers were allowed to set in a tissue culture incubator (30 min, 37 C, 5% C02), before being immersed in medium (Lonza EGM-2 unless indicated otherwise) and cultured for 2 days. Seeding protocol was identical for VE-cadherin blocked and chemically inhibited (ROCK, Rho, PAK-1, YAP-TEAD inhibitors) monolayers, except medium containing the relevant antibody/inhibitor was added 24 hours after seeding. For VE-cadherin block, B V9 blocking antibody in medium (Santa Cruz Biotechnology, 50 μg/mL, 16 hours incubation) was used. For cytoskeletal and YAP-TEAD inhibition, the following small molecule inhibitors were supplemented into medium: Y-27632 (Sigma Aldrich, 600 nM, ROCK inhibition), Rhosin (EMD Millipore, 10 μM, RhoA/B/C inhibition), IPA-3 (Sigma Aldrich, 5 μM, PAK-1 inhibition), Verteporfin (4 μM, YAP-TEAD inhibition). For YAP knockdown, YAP and control siRNA (Santa Cruz Biotechnology, sc-38637) were added to plated HUVEC using standard Attractene protocols. HUVEC were trypsinized and seeded onto ELP matrices two days after transfection to allow sufficient time for knockdown (Figure S13). For measurement of individual and collective EC motility, discrete monolayers were seeded as described above. After 24 hours culture, nuclei were labeled with NucBlue (2 drops per well, 10 min incubation) and EGM-2 medium supplemented with 10 μg/mL rutin (antioxidant compound that reduces phototoxicity). [55] Finally, for Western blots, single HUVEC monolayers were seeded onto matrices of varied fiber diameter in triplicate and cultured for 2 days.

Immunohistochemistry

HUVEC were fixed, permeabilized (0.05% v/v Triton X-100, 5 min) and blocked (1.5% w/v BSA, 30 min). BSA-diluted primary antibodies for VE-cadherin (polyclonal rabbit, Abcam, ab33168, 1/200 dilution), vinculin (clone hVin-1 mouse, Abcam, ab11194, 1/100 dilution), Ki67 (monoclonal mouse 8D5 or rabbit D3B5, Cell Signaling Technologies, 1/200 dilution), and YAP (mouse monoclonal 63.7, Santa Cruz Biotechnology, sc-101199, 1/400 dilution) were added and the samples were incubated at room temperature for 1 hr. Goat anti-mouse and anti-rabbit secondary antibodies conjugated to 633 and 550 nm DyLight fluorophores (Thermo Scientific, 1/200 dilution), respectively, were then added and the samples were again incubated at room temperature for 1 hr. After addition of phalloidin-488 (actin; 1/40 dilution in BSA, 15 min) and 2 drops of NucBlue (nucleus; 10 min), the samples were washed 4 times with 1.5% BSA, 10 min each. Coverslips with ELP matrices and stained HUVEC were mounted onto glass slides using Prolong Gold Antifade reagent without DAPI and imaged by confocal microscopy 24 hours later. To assess fiber width *in vivo*, 5 Fischer rats were euthanized and 1-cm lengths of aorta were immediately dissected, fixed in paraformaldehyde, embedded in gelatin, frozen, and cross-sectioned. All animals were handled according to the appropriate protocols, as defined by the Stanford Administrative Panel on Laboratory Animal Care. Aortic sections were then stained for elastin (clone C-21, Santa Cruz Biotechnology, sc-17581, 1/200 dilution) and actin (phalloidin-488, 1/40 dilution), labeled with anti-goat secondary antibody, and imaged by confocal microscopy.

Morphological characterization

All morphological features (*in vivo* and *in vitro* fiber width, *in vivo* and *in vitro* arc-chord ratio, and *in vitro* mean z-deviation of the basolateral cell membrane, cell spread area, and nuclear area) were measured using ImageJ. Junction disruption was quantified as 1 minus the average VE-cadherin junction length over total length of cell-cell contact. Total length of cell-cell contact was determined from manual tracing of the cell boundaries defined by actin co-staining. YAP nuclear localization was quantified by dividing the pixel intensity of immunostained YAP in the nucleus by intensity of YAP in the whole cell.

Western blot

After HUVEC culture, matrices were gently detached from coverslips and placed into 90 μL of lysis buffer (M-PER, Pierce) supplemented with protease inhibitor (1 μL Halt Cocktail, Thermo Scientific), phosphatase inhibitors (1 μL each of Cocktails 2 and 3, Sigma), sodium dodecyl sulfate and dithiothreitol. Matrices were then boiled (10 min) and sonicated (20 sec). Centrifugation (5 min, 4 C) was used to remove fabric from cell lysate. Separation was performed in polyacrylamide gels (4 hours, 140 kV) until the 20 kDa band eluted. Cold transfer buffer was prepared by mixing and chilling 200 mL 10x Tris-glycine, 400 mL methanol and 1400 mL water. Next, PVDF membranes were rinsed once with methanol, three times with water, and then once in cold transfer buffer for 5 min. Transfer sandwiches were assembled and proteins were transferred to PVDF membrane at 35 V for 16 hours on ice. For primary staining, membranes were washed with TBS (5 min), blocked with 5% dry milk in TBST (30 min) and then washes 2 times with TBST (5 min), before application of primary antibodies with 5% BSA in TBST (overnight incubation at 4 C, 1/1000 FAK/pFAK,

1/1000 ERK/pERK, 1/5000 glyceraldehyde 3-phosphate dehydrogenase, Cell Signaling Technologies; 1/1000 YAP, Santa Cruz Biotechnology). For secondary staining, membranes were washed vigorously in TBST on shaker incubators (5 min) before application of secondary antibodies in TBST (1/5000 HRP- labeled secondary antibodies, Cell Signaling Technologies). Finally, membranes were incubated in pico ECL (5 min) and exposed for 20 min on a BioRad ChemiDoc MP gel imager. Intensities of Western blot bands were normalized to intensity of bands produced from stains of glyceraldehyde 3-phosphate dehydrogenase (GAPDH). To calculate relative phosphoproteins, normalized intensity of phosphoprotein bands was divided by normalized intensity of total protein.

Endothelial cell motility

HUVEC were cultured into discrete monolayers on varied diameter ELP matrices and nuclear labeled as described above. Images of fibers and nuclei (DAPI filter) and fibers-only (Rhodamine filter) were taken every 20 min for 16 hours using a Zeiss Axiovision fluorescent microscope. Cell speed and centroid positions were calculated in Volocity using the default automated detection commands for cell nuclei (mean and standard error are for 600 cells over three independent view frames). Mean correlation was calculated from cell tracks according to the formula in Figure S9. Correlation distance was estimated by interpolating correlation as a function of radial distance r to calculate where the function equals zero.

Supplementary Material

Refer to Web version on PubMed Central for supplementary material.

Acknowledgments

This work was supported by the following grants: NIH F31-HL114315-01 (P.L.B.), Stanford Bio-X Undergraduate Summer Research Program (S.M.), National Defense Science and Engineering Graduate Fellowship (A.C.P.), NIH F31 EB020502-01 (C.M.M.), NSF DMR 1508006, NIH R21 EB018407, NIH U19 AI116484, (S.C.H.), NIH T32 GM008294 (K.H.H.).

References

1. Alberts, B. Molecular Biology of the Cell. Garland Science; New York: 2002. The Extracellular Matrix of Animals.
2. Davis GE, Senger DR. Endothelial extracellular matrix: biosynthesis remodeling and functions during vascular morphogenesis and neovessel stabilization. Circulation research. 2005; 97(11): 1093–1107. [PubMed: 16306453]
3. Baker BM, Trappmann B, Wang WY, Sakar MS, Kim IL, Shenoy VB, Burdick JA, Chen CS. Cell-mediated fibre recruitment drives extracellular matrix mechanosensing in engineered fibrillar microenvironments. Nature materials. 2015; 14(12):1262–1268. [PubMed: 26461445]
4. Discher DE, Janmey P, Wang YL. Tissue cells feel and respond to the stiffness of their substrate. Science. 2005; 310(5751):1139–1143. [PubMed: 16293750]
5. Yeung T, Georges PC, Flanagan LA, Marg B, Ortiz M, Funaki M, Zahir N, Ming W, Weaver V, Janmey PA. Effects of substrate stiffness on cell morphology cytoskeletal structure and adhesion. Cell motility and the cytoskeleton. 2005; 60(1):24–34. [PubMed: 15573414]
6. Benitez PL, Mascharak S, Proctor AC, Heilshorn SC. Use of protein-engineered fabrics to identify design rules for integrin ligand clustering in biomaterials. Integrative biology : quantitative biosciences from nano to macro. 2016; 8(1):50–61. [PubMed: 26692238]

7. Baker BM, Chen CS. Deconstructing the third dimension: how 3D culture microenvironments alter cellular cues. Journal of cell science. 2012; 125(Pt 13):3015–3024. [PubMed: 22797912]
8. Rosenbloom J, Abrams WR, Mecham R. Extracellular matrix 4: the elastic fiber. FASEB journal : official publication of the Federation of American Societies for Experimental Biology. 1993; 7(13): 1208–1218. [PubMed: 8405806]
9. Farand P, Garon A, Plante GE. Structure of large arteries: orientation of elastin in rabbit aortic internal elastic lamina and in the elastic lamellae of aortic media. Microvascular research. 2007; 73(2):95–99. [PubMed: 17174983]
10. Ushiki T. Collagen fibers reticular fibers and elastic fibers. A comprehensive understanding from a morphological viewpoint. Archives of histology and cytology. 2002; 65(2):109–126. [PubMed: 12164335]
11. Metavarayuth KSP, Zhao X, Lin Y, Wang Q. Influence of Surface Topographical Cues on the Differentiation of Mesenchymal Stem Cells in Vitro. ACS Biomater. Sci. Eng. 2016; 2(2):142–151.
12. Nikkhah M, Edalat F, Manoucheri S, Khademhosseini A. Engineering microscale topographies to control the cell-substrate interface. Biomaterials. 2012; 33(21):5230–5246. [PubMed: 22521491]
13. Potthoff E, Franco D, D'Alessandro V, Starck C, Falk V, Zambelli T, Vorholt JA, Poulikakos D, Ferrari A. Toward a rational design of surface textures promoting endothelialization. Nano letters. 2014; 14(2):1069–1079. [PubMed: 24428164]
14. Kim DH, Provenzano PP, Smith CL, Levchenko A. Matrix nanotopography as a regulator of cell function. The Journal of cell biology. 2012; 197(3):351–360. [PubMed: 22547406]
15. Le Saux G, Magenau A, Bocking T, Gaus K, Gooding JJ. The relative importance of topography and RGD ligand density for endothelial cell adhesion. PloS one. 2011; 6(7):e21869. [PubMed: 21779342]
16. Benitez PL, Sweet JA, Fink H, Chennazhi KP, Nair SV, Enejder A, Heilshorn SC. Sequence-specific crosslinking of electrospun elastin-like protein preserves bioactivity and native-like mechanics. Advanced healthcare materials. 2013; 2(1):114–118. [PubMed: 23184558]
17. Straley KSHSC. Independent tuning of multiple biomaterial properties using protein engineering. Soft Matter. 2009; 5:114–124.
18. Fong E, Tzlil S, Tirrell DA. Boundary crossing in epithelial wound healing. Proceedings of the National Academy of Sciences of the United States of America. 2010; 107(45):19302–19307. [PubMed: 20974917]
19. Liu JC, Tirrell DA. Cell response to RGD density in cross-linked artificial extracellular matrix protein films. Biomacromolecules. 2008; 9(11):2984–2988. [PubMed: 18826275]
20. Zheng W, Wang Z, Song L, Zhao Q, Zhang J, Li D, Wang S, Han J, Zheng XL, Yang Z, Kong D. Endothelialization and patency of RGD-functionalized vascular grafts in a rabbit carotid artery model. Biomaterials. 2012; 33(10):2880–2891. [PubMed: 22244694]
21. Zhou J, Nie B, Zhu Z, Ding J, Yang W, Shi J, Dong X, Xu J, Dong N. Promoting endothelialization on decellularized porcine aortic valve by immobilizing branched polyethylene glycolmodified with cyclic-RGD peptide: an in vitro study. Biomed Mater. 2015; 10(6):065014. [PubMed: 26584634]
22. de Mel A, Punshon G, Ramesh B, Sarkar S, Darbyshire A, Hamilton G, Seifalian AM. In situ endothelialization potential of a biofunctionalised nanocomposite biomaterial-based small diameter bypass graft. Biomed Mater Eng. 2009; 19(4–5):317–331. [PubMed: 20042799]
23. Kang TY, Lee JH, Kim BJ, Kang JA, Hong JM, Kim BS, Cha HJ, Rhie JW, Cho DW. In vivo endothelization of tubular vascular grafts through in situ recruitment of endothelial and endothelial progenitor cells by RGD-fused mussel adhesive proteins. Biofabrication. 2015; 7(1):015007. [PubMed: 25599716]
24. Blindt R, Vogt F, Astafieva I, Fach C, Hristov M, Krott N, Seitz B, Kapurniotu A, Kwok C, Dewor M, Bosserhoff AK, Bernhagen J, Hanrath P, Hoffmann R, Weber C. A novel drug-eluting stent coated with an integrin-binding cyclic Arg-Gly-Asp peptide inhibits neointimal hyperplasia by recruiting endothelial progenitor cells. J Am Coll Cardiol. 2006; 47(9):1786–1795. [PubMed: 16682302]

25. Arnold M, Cavalcanti-Adam EA, Glass R, Blummel J, Eck W, Kantlehner M, Kessler H, Spatz JP. Activation of integrin function by nanopatterned adhesive interfaces. Chemphyschem : a European journal of chemical physics and physical chemistry. 2004; 5(3):383–388. [PubMed: 15067875]
26. Maheshwari G, Brown G, Lauffenburger DA, Wells A, Griffith LG. Cell adhesion and motility depend on nanoscale RGD clustering. Journal of cell science. 2000; 113(Pt 10):1677–1686. [PubMed: 10769199]
27. Sazonova OV, Lee KL, Isenberg BC, Rich CB, Nugent MA, Wong JY. Cell-cell interactions mediate the response of vascular smooth muscle cells to substrate stiffness. Biophysical journal. 2011; 101(3):622–630. [PubMed: 21806930]
28. Pelham RJ Jr, Wang Y. Cell locomotion and focal adhesions are regulated by substrate flexibility. Proceedings of the National Academy of Sciences of the United States of America. 1997; 94(25): 13661–13665. [PubMed: 9391082]
29. Bergel DH. The static elastic properties of the arterial wall. The Journal of physiology. 1961; 156(3):445–457. [PubMed: 16992075]
30. Orsenigo F, Giampietro C, Ferrari A, Corada M, Galaup A, Sigismund S, Ristagno G, Maddaluno L, Koh GY, Franco D, Kurtcuoglu V, Poulikakos D, Baluk P, McDonald D, Grazia Lampugnani M, Dejana E. Phosphorylation of VE-cadherin is modulated by haemodynamic forces and contributes to the regulation of vascular permeability in vivo. Nature communications. 2012; 3:1208.
31. Giampietro C, Disanza A, Bravi L, Barrios-Rodiles M, Corada M, Frittoli E, Savorani C, Lampugnani MG, Boggetti B, Niessen C, Wrana JL, Scita G, Dejana E. The actin-binding protein EPS8 binds VE-cadherin and modulates YAP localization and signaling. The Journal of cell biology. 2015; 211(6):1177–1192. [PubMed: 26668327]
32. Lampugnani MG, Corada M, Andriopoulou P, Esser S, Risau W, Dejana E. Cell confluence regulates tyrosine phosphorylation of adherens junction components in endothelial cells. Journal of cell science. 1997; 110(Pt 17):2065–2077. [PubMed: 9378757]
33. Millan J, Cain RJ, Reglero-Real N, Bigarella C, Marcos-Ramiro B, Fernandez-Martin L, Correas I, Ridley AJ. Adherens junctions connect stress fibres between adjacent endothelial cells. BMC biology. 2010; 8:11. [PubMed: 20122254]
34. Lampugnani MG. Endothelial adherens junctions and the actin cytoskeleton: an ‘infinity net’? Journal of biology. 2010; 9(3):16. [PubMed: 20377920]
35. Murrell M, Oakes PW, Lenz M, Gardel ML. Forcing cells into shape: the mechanics of actomyosin contractility. Nature reviews. Molecular cell biology. 2015; 16(8):486–98. [PubMed: 26130009]
36. Khatau SB, Hale CM, Stewart-Hutchinson PJ, Patel MS, Stewart CL, Searson PC, Hodzic D, Wirtz D. A perinuclear actin cap regulates nuclear shape. Proceedings of the National Academy of Sciences of the United States of America. 2009; 106(45):19017–22. [PubMed: 19850871]
37. Wallez Y, Vilgrain I, Huber P. Angiogenesis: the VE-cadherin switch. Trends in cardiovascular medicine. 2006; 16(2):55–59. [PubMed: 16473763]
38. Dejana E. Endothelial adherens junctions: implications in the control of vascular permeability and angiogenesis. The Journal of clinical investigation. 1996; 98(9):1949–53. [PubMed: 8903311]
39. Amano M, Nakayama M, Kaibuchi K. Rho-kinase/ROCK: A key regulator of the cytoskeleton and cell polarity. Cytoskeleton. 2010; 67(9):545–554. [PubMed: 20803696]
40. Mooney DJ, Langer R, Ingber DE. Cytoskeletal filament assembly and the control of cell spreading and function by extracellular matrix. Journal of cell science. 1995; 108(Pt 6):2311–2320. [PubMed: 7673351]
41. Chaudhuri O, Gu L, Darnell M, Klumpers D, Bencherif SA, Weaver JC, Huebsch N, Mooney DJ. Substrate stress relaxation regulates cell spreading. Nature communications. 2015; 6:6364.
42. Rudini N, Felici A, Giampietro C, Lampugnani M, Corada M, Swirsding K, Garre M, Liebner S, Letarte M, ten Dijke P, Dejana E. VE-cadherin is a critical endothelial regulator of TGF-beta signalling. The EMBO journal. 2008; 27(7):993–1004. [PubMed: 18337748]
43. Potter MD, Barbero S, Cheresh DA. Tyrosine phosphorylation of VE-cadherin prevents binding of p120- and beta-catenin and maintains the cellular mesenchymal state. The Journal of biological chemistry. 2005; 280(36):31906–31912. [PubMed: 16027153]

44. Choi HJ, Zhang H, Park H, Choi KS, Lee HW, Agrawal V, Kim YM, Kwon YG. Yes-associated protein regulates endothelial cell contact-mediated expression of angiopoietin-2. Nature communications. 2015; 6:6943.
45. Li Z, Zhao B, Wang P, Chen F, Dong Z, Yang H, Guan KL, Xu Y. Structural insights into the YAP and TEAD complex. Genes & development. 2010; 24(3):235–240. [PubMed: 20123905]
46. Liu-Chittenden Y, Huang B, Shim JS, Chen Q, Lee SJ, Anders RA, Liu JO, Pan D. Genetic and pharmacological disruption of the TEAD-YAP complex suppresses the oncogenic activity of YAP. Genes & development. 2012; 26(12):1300–1305. [PubMed: 22677547]
47. Zhang W, Liu HT. MAPK signal pathways in the regulation of cell proliferation in mammalian cells. Cell research. 2002; 12(1):9–18. [PubMed: 11942415]
48. Huang C, Jacobson K, Schaller MD. MAP kinases and cell migration. Journal of cell science. 2004; 117(Pt 20):4619–4628. [PubMed: 15371522]
49. Schwartz MP, Hou Z, Propson NE, Zhang J, Engstrom CJ, Santos Costa V, Jiang P, Nguyen BK, Bolin JM, Daly W, Wang Y, Stewart R, Page CD, Murphy WL, Thomson JA. Human pluripotent stem cell-derived neural constructs for predicting neural toxicity. Proceedings of the National Academy of Sciences of the United States of America. 2015; 112(40):12516–12521. [PubMed: 26392547]
50. Serbo JV, Gerecht S. Vascular tissue engineering: biodegradable scaffold platforms to promote angiogenesis. Stem Cell Res Ther. 2013; 4(1):8. [PubMed: 23347554]
51. Lesman A, Gepstein L, Levenberg S. Vascularization shaping the heart. Ann N Y Acad Sci. 2010; 1188:46–51. [PubMed: 20201885]
52. Rangamani P, Mandadap KK, Oster G. Protein-induced membrane curvature alters local membrane tension. Biophysical journal. 2014; 107(3):751–762. [PubMed: 25099814]
53. Shattil SJ, Newman PJ. Integrins: dynamic scaffolds for adhesion and signaling in platelets. Blood. 2004; 104(6):1606–1615. [PubMed: 15205259]
54. Trepat XWMR, Angelini TE, Millet E, Weitz DA, Butler JP, Fredberg JJ. Physical forces during collective cell migration. Nat. Phys. 2009; 5:426–430.
55. Bogdanov AM, Kudryavtseva EI, Lukyanov KA. Anti-fading media for live cell GFP imaging. PloS one. 2012; 7(12):e53004. [PubMed: 23285248]

Impact Statement

A mechanotransduction mechanism linking native-like substrate topography to endothelial cell migration and proliferation is presented. To elucidate this mechanism, a recombinant electrospun elastin-like protein system with independently tunable, native-like topography is designed. The findings in this work expand current understanding of topography-induced cell responses and establish topography as a critical design parameter for biomaterials.

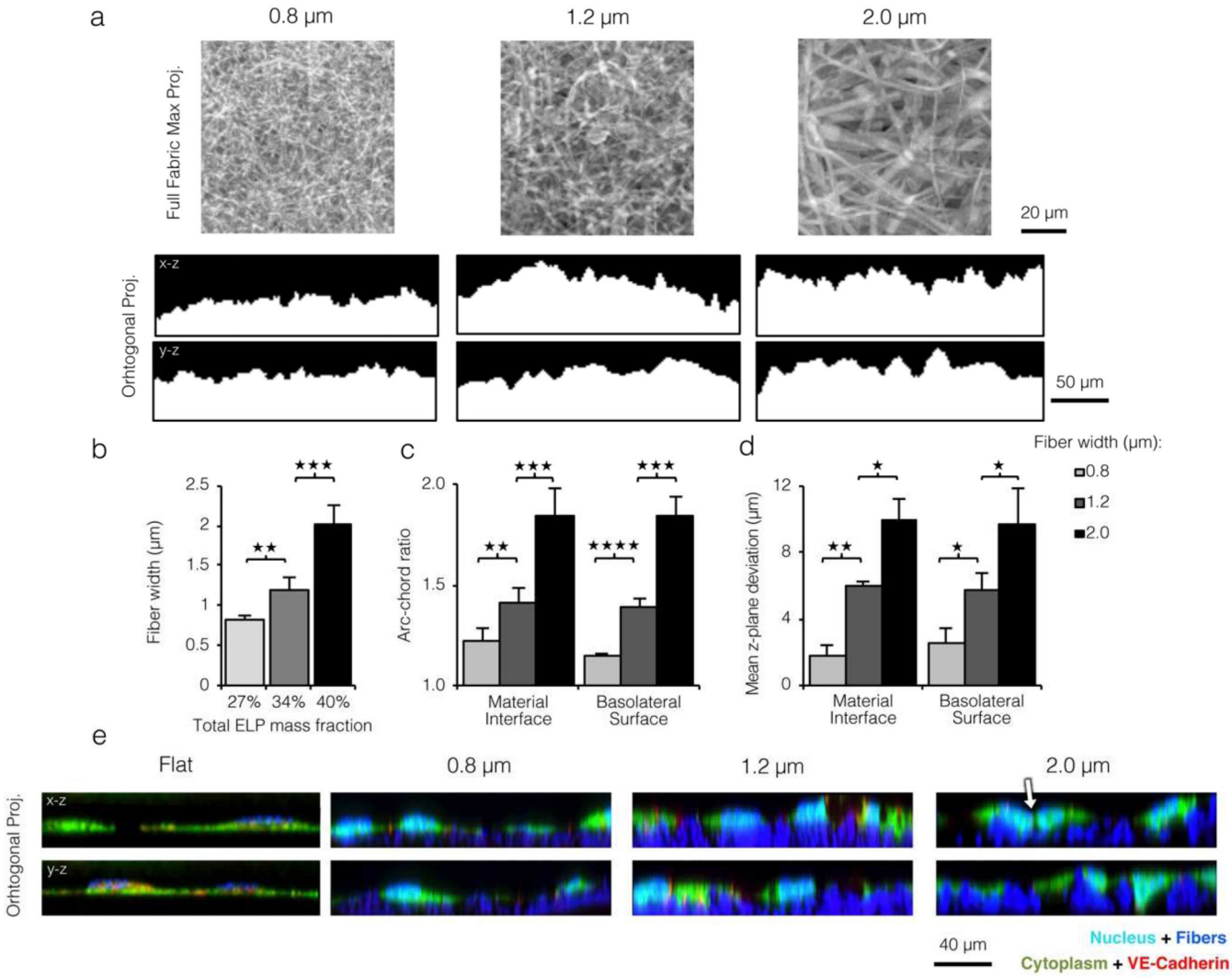

Figure 1. ELP matrices of larger fiber width present endothelial cells with more varied substrate topography

a) Top: Confocal microscopy max projections of electrospun ELP matrices. Bottom: x-z and y-z orthogonal projections of confocal z-stacks taken for ELP matrices with varied fiber width. Increased fiber width yielded a less planar material interface. b) Left: Mean fiber widths electrospun from precursor solutions with varied ELP mass fraction. Increasing total ELP mass fraction in the aqueous precursor solution (27 to 42% w/w) yielded wider fibers (0.8 to 2.0 μ mean width). c) Topographical variation of ELP substrates quantified as arc-chord ratio (Figure S4 top panel). d) Topographical variation of ELP substrates quantified as average z-variance from the mean (Figure S4 bottom panel). For both quantification schemes c and d, increased fiber width led to more pronounced topographical variation of the substrate and EC basolateral surface. e) Orthogonal projections of ECs cultured on ELP flat control and fibrous matrices and stained for the nucleus (cyan), cytoplasm (green), and VE-cadherin (red); fibers appear blue. ECs on the planar control and on small width fibers maintained a planar basolateral surface while ECs on larger width fibers closely followed the topographical variation of the underlying matrix. Basolateral membrane deformation was

accompanied by loss of VE-cadherin at cell-cell junctions (white arrow). (* $p < 0.05$, ** $p < 0.01$, *** $p < 0.001$, **** $p < 10^{-4}$)

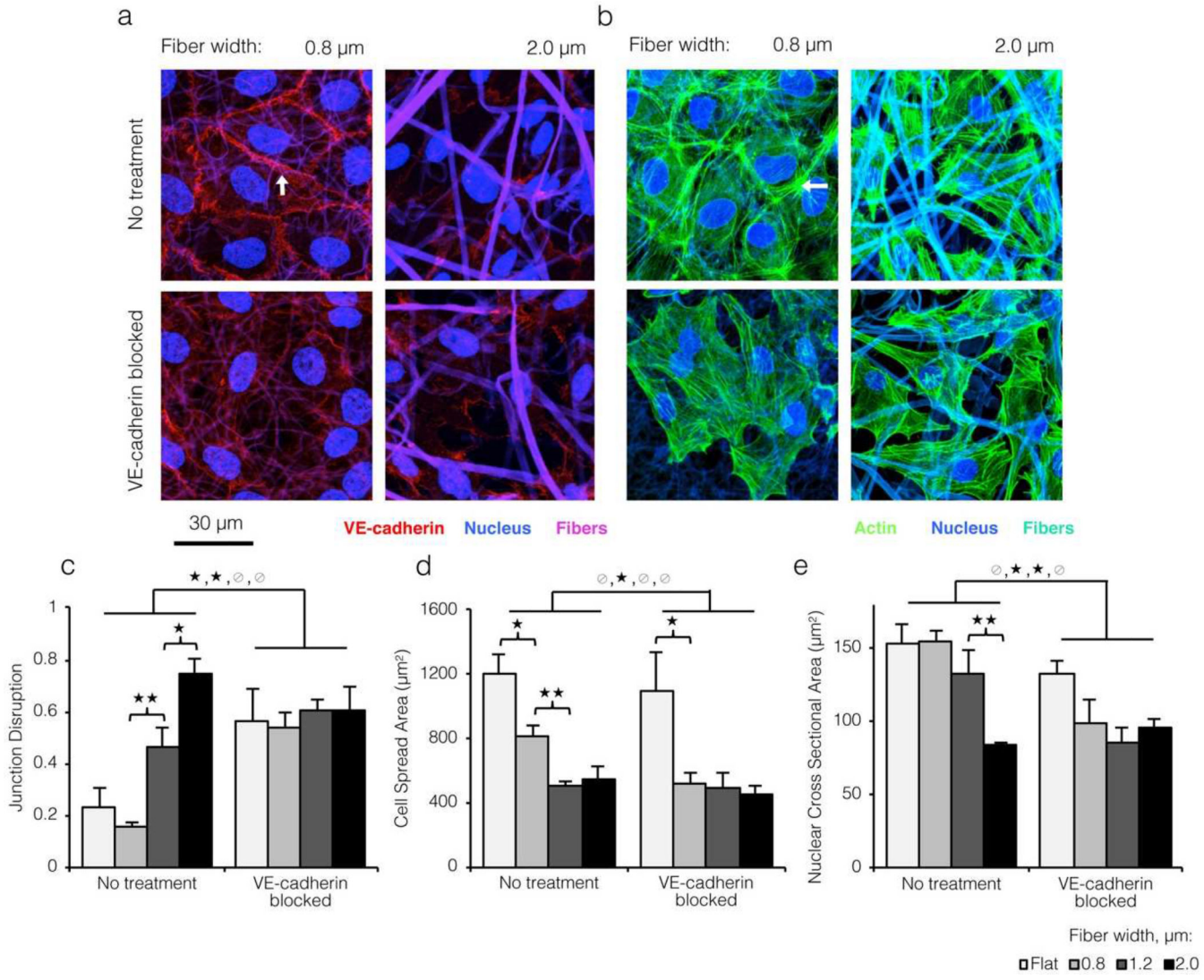

Figure 2. Loss of VE-cadherin on topographically varied substrates causes morphological changes indicative of increased cytoskeletal contractility

a) Confocal images of ECs cultured on varied width ELP fibers and immunostained for VE-cadherin (red; stable junction indicated by white arrow) and the nucleus (blue). Fibers shown in violet. ECs on larger width fibers showed disruption of VE-cadherin junctions reminiscent of the effects of a VE-cadherin blocking antibody. b) ECs cultured on varied width ELP fibers and stained for the actin cytoskeleton (green) and nucleus (blue). Fibers shown in cyan. Strong cortical arcs of actin (white arrow) suggested low cytoskeletal contractility and stable junctions on small width ELP fibers. Conversely, ECs on larger width fibers showed strong transverse actin filaments, as did ECs on all substrates after VE-cadherin blocking. c) Quantification of cell-cell junction disruption for ECs cultured on varied topographies with and without VE-cadherin blocking (see Experimental Section). d,e) Decreased cell spreading and nuclear area indicated greater contractile forces on larger width fibers. These data indicate that loss of VE-cadherin on more topographically varied substrates is sufficient to alter actin morphology and contractility. (* $p < 0.05$, **$p<0.01$)

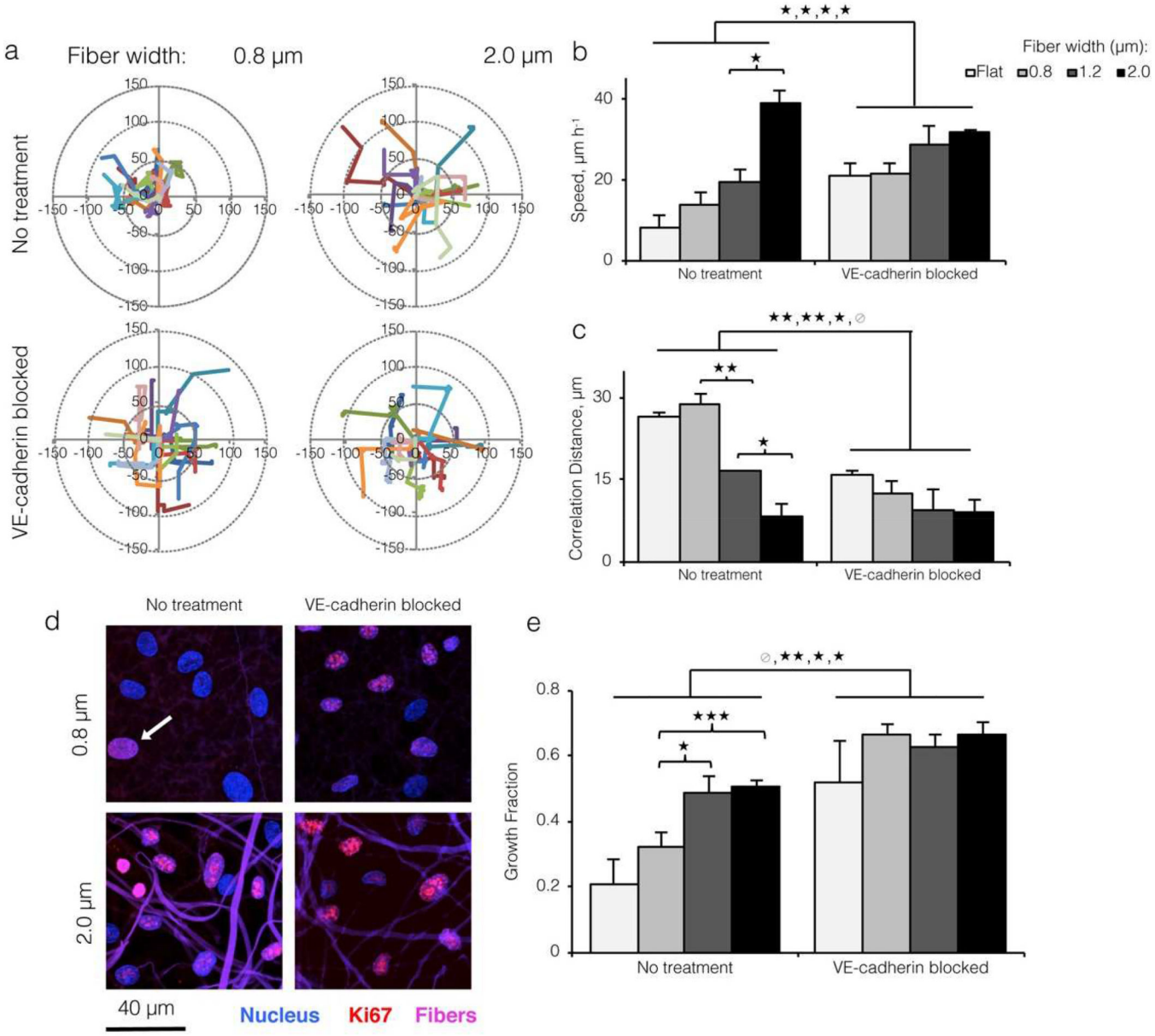

Figure 3. Topographical variation promotes endothelial cell migration and proliferation through disruption of VE-cadherin junctions

a) Motility track plots of ECs cultured on ELP fabrics with varied fiber widths, with and without VE-cadherin blocking antibody (15 representative tracks per condition shown; 600 cells tracked for 16 hours per condition). b) Average motility speed quantified from tracks. ECs migrated at a faster speed on larger fibers and on all substrates after VE-cadherin blocking, consistent with a loss of contact inhibition by VE-cadherin. c) Correlation distance (mean radial distance at which mean cell-cell correlation equals 0; see Figure S9) decreased with increasing fiber width and after VE-cadherin blocking, indicating a loss of contact guidance by VE-cadherin on topographically varied substrates. d) Confocal images of ECs cultured on varied width ELP fibers with and without VE-cadherin blocking antibody, and stained for Ki67 (red; positive cell indicated by white arrow) and nuclei (blue). Fibers shown

in violet. e) Quantification of Ki67 growth fraction per culture condition showed a VE-cadherin dependent increase in proliferation on larger width ELP fibers. (* $p < 0.05$, ** $p < 0.01$,*** $p < 0.001$)

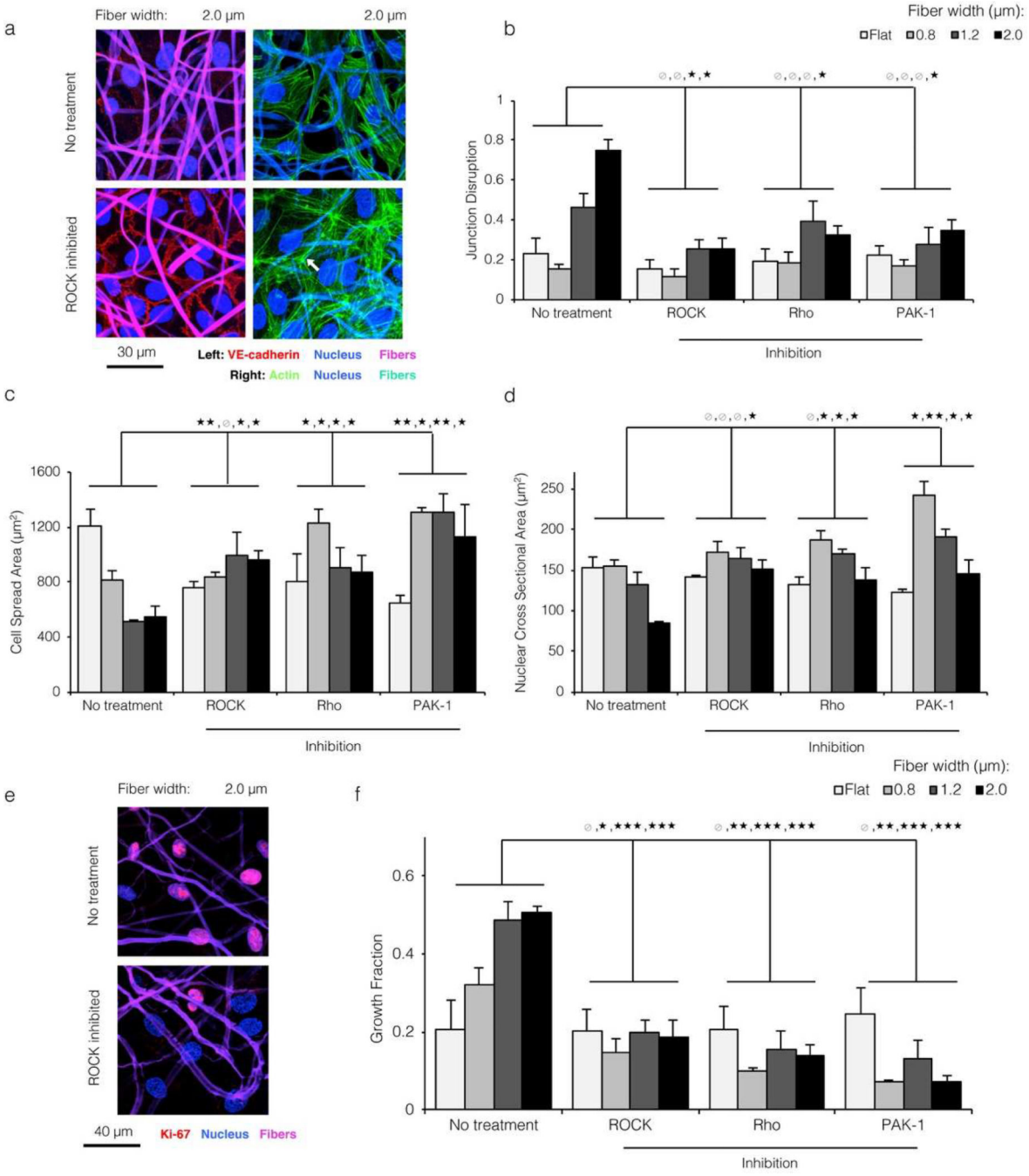

Figure 4. Topographical cues modulating EC morphology and proliferation are dependent on Rho, ROCK, and Rac signaling

a) ECs cultured on the most topographically varied substrate (2.0 μ wide fibers), treated with ROCK inhibitor Y-27632, and stained for the nucleus (blue) and VE-cadherin (red) or actin (green). Fibers are shown in violet (left panels) or cyan (right panels). Chemical inhibition of cytoskeletal signaling prevented both the loss of VE-cadherin junctions and the reorganization of actin away from junctions (white arrow), despite the underlying substrate topography. b,c,d) For all topographical conditions, chemical inhibition of Rho, ROCK, and Rac signaling led to EC morphology reminiscent of that on flat and small width fibrous

substrates: low junction disruption (b), large planar spreading area (c), and large nuclear area (d). This suggested that the morphological shifts associated with more varied substrate topography were dependent on cytoskeletal signaling. e,f) ECs cultured on large width ELP fibers and treated with cytoskeletal inhibitors proliferated at a low level, consistent with a regain of contact inhibition by VE-cadherin. (* $p < 0.05$, ** $p < 0.01$, *** $p < 0.001$)

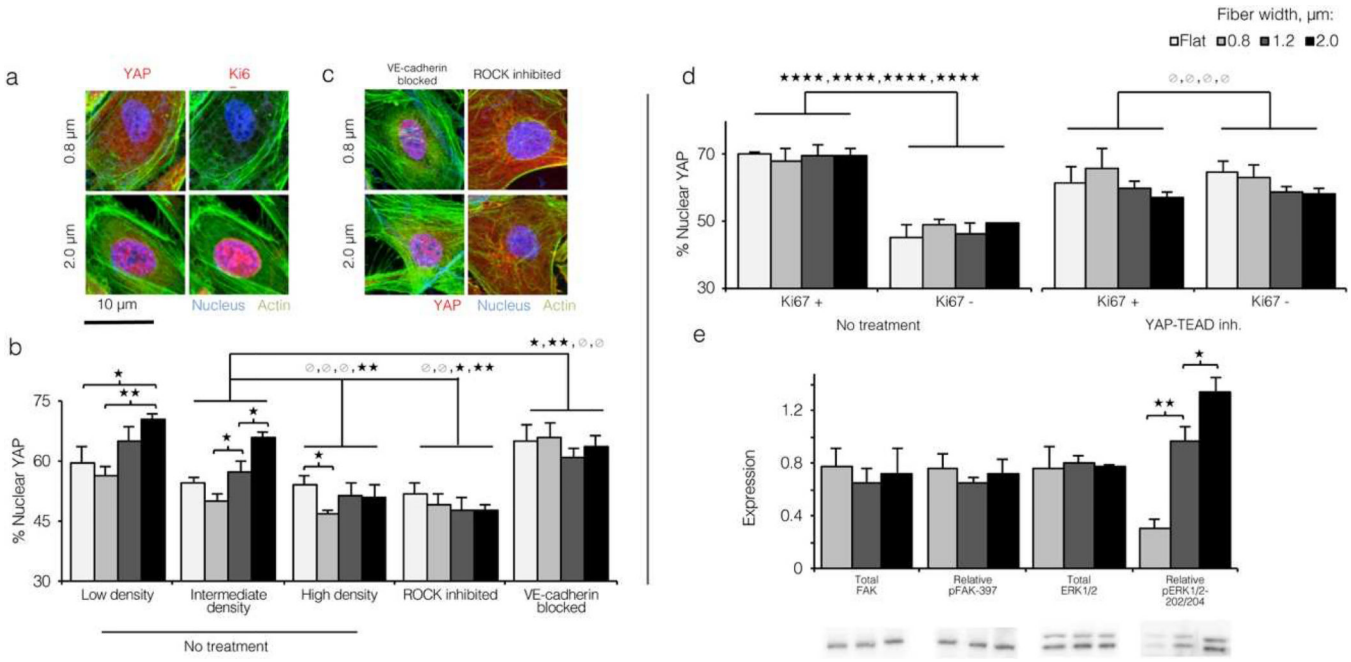

Figure 5. Loss of cell-cell contact on topographically varied ELP substrates drives nuclear translocation of YAP

a) Confocal images of ECs cultured on 0.8 and 2.0 μm wide ELP fibers and immunostained for nuclei (blue), actin (green), and YAP (left panels, red) or Ki67 (right panels, red). Proliferative ECs on larger width fibers appeared to show greater localization of YAP to the nucleus, b) Pixel intensity-based quantification of YAP nuclear localization (see Experimental Section) for ECs cultured on all topographies at varied density, and after treatment with ROCK inhibitor or VE-cadherin blocking antibody. Disruption of VE-cadherin with a blocking antibody increased YAP nuclear localization; conversely, cytoskeletal inhibition decreased nuclear YAP localization. c) Confocal images of ECs cultured on varied topographies, treated with VE-cadherin blocking antibody or cytoskeletal signaling inhibitor Y-27632, and immunostained as in panel a. d) Quantification of YAP nuclear localization for Ki67+ and Ki67- ECs with and without YAP-TEAD inhibitor Verteporfin. YAP-TEAD inhibition decoupled nuclear YAP localization to cell cycle entry, as inferred by the fact that Ki67+ and Ki67- cells showed similar degrees of nuclear YAP localization across all topographies. e) Expression and phosphorylation of FAK and ERK1/2 assayed by Western blot. Expression and phosphorylation of FAK was unaffected by substrate topography, while ERK1/2 phosphorylation was significantly higher on more topographically varied ELP substrates. (* $p < 0.05$, ** $p < 0.01$, *** $p < 0.001$, **** $p < 10^{-4}$)

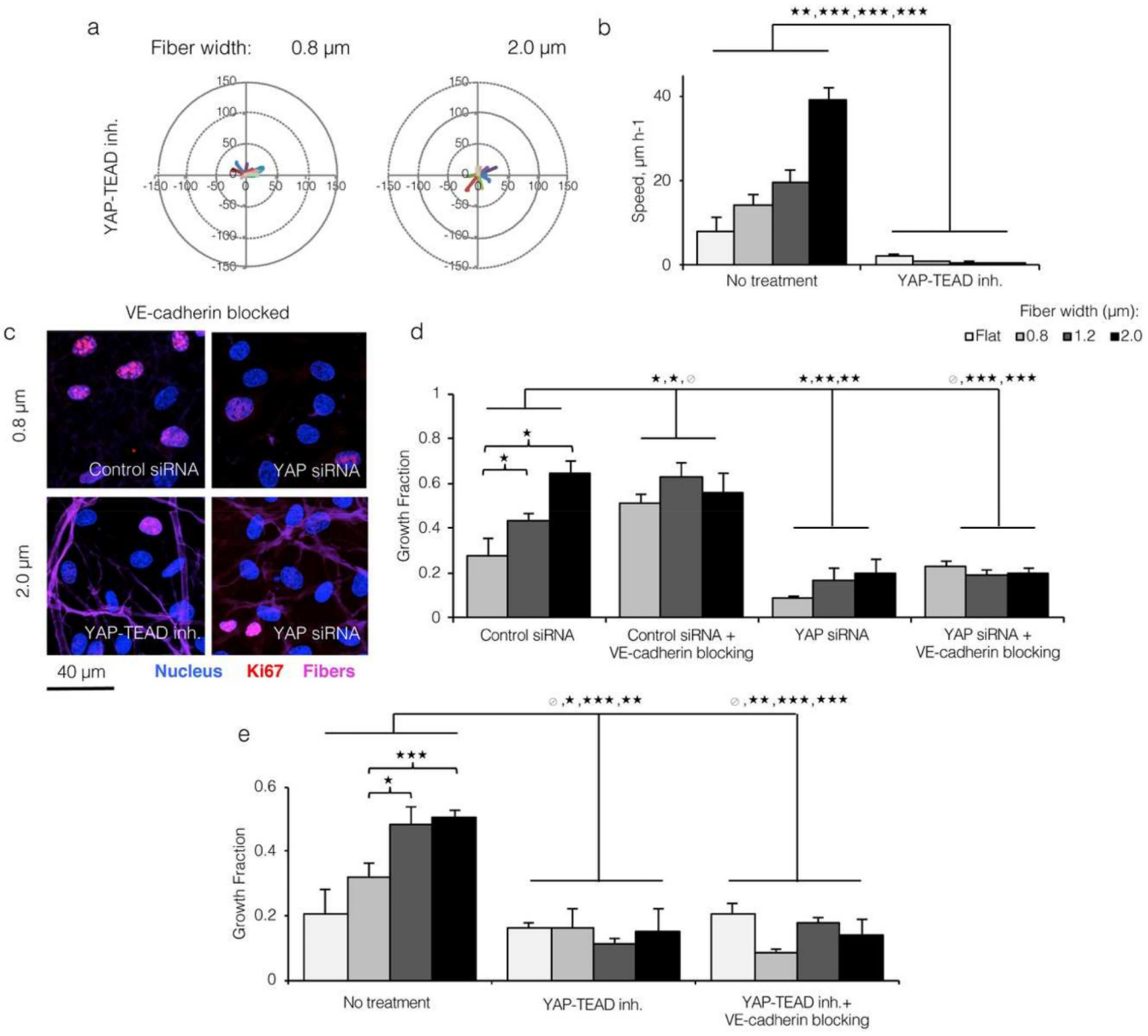

Figure 6. Endothelial migration and proliferation in response to topographical variation requires YAP-TEAD interaction

a) Motility track plots of ECs cultured on ELP fabrics with varied fiber widths and treated with YAP-TEAD inhibitor Verteporfin (15 representative tracks per condition; 600 cells tracked for 16 hours). b) ECs with inhibited YAP-TEAD interactions moved significantly slower, confirming YAP's role in cellular motility. c) ECs cultured onto varied width ELP fibers, treated with VE-cadherin blocking antibody, and stained for Ki67 after YAP knockdown or chemical YAP-TEAD inhibition. d,e) YAP knockdown and YAP-TEAD chemical inhibition both blocked EC proliferation in response to varied substrate topography and VE-cadherin blocking antibody, suggesting that YAP activation is required for topography-mediated cell cycle entry. (* $p < 0.05$, ** $p < 0.01$, *** $p < 0.001$)